DENSITY-FUNCTIONAL APPROACH TO ATOMS IN STRONG LASER PULSES

C. A. ULLRICH, S. ERHARD and E. K. U. GROSS
Institut für Theoretische Physik
Universität Würzburg
Am Hubland
D-97074 Würzburg
Germany

1. Introduction

The basic idea of density functional theory (DFT) is to describe an interacting many-particle system exclusively and completely in terms of its density. The formalism rests on two basic theorems:

I. Every observable quantity can be calculated, at least in principle, from the density alone, i. e. each quantum mechanical observable can be written as a functional of the density.

II. The density of the interacting system of interest can be obtained as density of an auxiliary system of non-interacting particles moving in an effective *local* single-particle potential (the so-called Kohn-Sham potential).

In the original work of Hohenberg, Kohn and Sham [1, 2] these theorems were proven for the ground-state density of *static* many-body systems. On the basis of these theorems, DFT has provided an extremely successful description of ground-state properties of atoms, molecules and solids [3, 4]. The accuracy of approximations for the Kohn-Sham potential has steadily improved over the years and the currently best functionals yield ground-state properties in very close agreement with configuration interaction results [5].

DFT of time-dependent systems (TDDFT) is a more recent development [6]–[8]. The important theorems I and II stated above have been shown to hold true for the time-dependent density as well [6]. So far, TDDFT has been applied almost exclusively in the regime of linear response (for recent reviews see, e. g., Refs. [7]–[9]).

In this paper, TDDFT is used to study the interaction of atoms with very strong laser pulses having intensities that require a non-perturbative treatment of the laser field. Many authors have attacked this problem with a variety of techniques [10, 11]. Often the electronic motion has been treated classically or semiclassically. Most of the quantum mechanical work was either done on the hydrogen atom or

on rare gas atoms within a single-active-electron model. The principal advantage of TDDFT is that it provides a fully quantum mechanical approach that incorporates correlation effects due to the electron-electron interaction in a systematic fashion. The interacting many-body problem is mapped on an auxiliary system of non-interacting particles moving in an effective time-dependent potential. Since this potential is *local* in configuration space the resulting numerical scheme is less involved than the time-dependent Hartree-Fock (TDHF) method. In section 2, we give an overview of TDDFT. In sections 3 and 4 numerical results on multiphoton ionization and harmonic generation of helium and neon will be presented.

2. Time-dependent density functional formalism

We study the time evolution of a system of N electrons governed by the time-dependent Schrödinger equation

$$i\frac{\partial}{\partial t}\Phi(t) = \hat{H}(t)\Phi(t) \tag{1}$$

(atomic [Hartree] units are used throughout). The total Hamiltonian, written in second quantized notation, is given by

$$\hat{H}(t) = \hat{T} + \hat{W} + \hat{V}(t) \quad , \tag{2}$$

where $\hat{T}$ is the kinetic energy of the electrons,

$$\hat{T} = \sum_{\sigma=\uparrow\downarrow} \int d^3r\ \hat{\psi}^\dagger_\sigma(\mathbf{r}) \left(-\frac{\nabla^2}{2}\right) \hat{\psi}_\sigma(\mathbf{r}) \quad , \tag{3}$$

and $\hat{W}$ is the mutual Coulomb interaction,

$$\hat{W} = \frac{1}{2}\sum_{\sigma,\sigma'} \int d^3r \int d^3r'\ \hat{\psi}^\dagger_\sigma(\mathbf{r})\hat{\psi}^\dagger_{\sigma'}(\mathbf{r}')\frac{1}{|\mathbf{r}-\mathbf{r}'|}\hat{\psi}_{\sigma'}(\mathbf{r}')\hat{\psi}_\sigma(\mathbf{r}) \quad . \tag{4}$$

The electrons move in an explicitly time-dependent external potential

$$\hat{V}(t) = \int d^3r\ v_{\text{ext}}(\mathbf{r}t)\hat{n}(\mathbf{r}) \quad , \tag{5}$$

where $\hat{n}(\mathbf{r})$ is the density operator

$$\hat{n}(\mathbf{r}) = \sum_{\sigma=\uparrow\downarrow} \hat{\psi}^\dagger_\sigma(\mathbf{r})\hat{\psi}_\sigma(\mathbf{r}) \quad . \tag{6}$$

Generally the external potential $v_{\text{ext}}(\mathbf{r}t)$ consists of a static contribution (e. g., the nuclear Coulomb potential) and a time-dependent part (e. g., the laser field).

Time-dependent density functional theory is based on the existence of an exact one-to-one mapping between time-dependent densities and external potentials. We investigate the densities $n(\mathbf{r}t)$ of electronic systems evolving from a *fixed* initial (many-particle) state $\Phi(t_0) = \Phi_0$ under the influence of different external poten-

tials $v_{\rm ext}(\mathbf{r}t)$. Each external potential leads, via solution of the time-dependent Schrödinger equation (1), to a time-dependent many-body wave function $\Phi(t)$. For a fixed initial state Φ_0, this defines a map

$$\mathcal{A} : v_{\rm ext}(\mathbf{r}t) \longrightarrow \Phi(t) \tag{7}$$

between the external potentials and the corresponding time-dependent many-particle wave functions. By virtue of the density operator (6), a second map

$$\mathcal{B} : \Phi(t) \longrightarrow n(\mathbf{r}t) = \langle \Phi(t) | \hat{n}(\mathbf{r}) | \Phi(t) \rangle \tag{8}$$

is established between the many-particle wave functions and the time-dependent densities. The heart of TDDFT is the proof of invertibility of the combined map $\mathcal{G} \equiv \mathcal{B} \circ \mathcal{A}$:

$$\mathcal{G} : v_{\rm ext}(\mathbf{r}t) \longrightarrow n(\mathbf{r}t) \quad . \tag{9}$$

The invertibility of this map was first proven by Runge and Gross [6]. These authors demonstrated that two densities $n(\mathbf{r}t)$ and $n'(\mathbf{r}t)$ evolving from a common initial state Φ_0 under the influence of two potentials $v_{\rm ext}(\mathbf{r}t)$ and $v'_{\rm ext}(\mathbf{r}t)$ always become different infinitesimally later than t_0, provided that the potentials differ by more than a purely time-dependent function $c(t)$. The set of potentials for which invertibility can be shown comprises all potentials expandable in a Taylor series with respect to the time coordinate around the initial time t_0. Having established the existence of the inverse map

$$\mathcal{G}^{-1} : n(\mathbf{r}t) \longrightarrow v_{\rm ext}(\mathbf{r}t) + c(t) \quad , \tag{10}$$

subsequent application of the map $\mathcal{A}$ tells us that the full many-particle wave function is a functional of the time-dependent density, unique up to within a purely time-dependent phase $\alpha(t)$:

$$\Phi(t) = e^{-i\alpha(t)} \Psi[n](t) \quad . \tag{11}$$

As a consequence, the expectation value of any quantum mechanical operator $\hat{Q}(t)$ is a *unique* functional of the density:

$$Q[n](t) = \langle \Psi[n](t) | \hat{Q}(t) | \Psi[n](t) \rangle \quad . \tag{12}$$

The ambiguity in the phase cancels out (provided that $\hat{Q}(t)$ contains no time derivatives). This proves theorem I stated in the introduction. Some quantities (such as harmonic spectra) are easily calculated from the time-dependent density, while other quantities (such as ATI spectra) are difficult to extract from the density. But, as a matter of principle, *all* physical observables are determined by the time-dependent density alone, once the initial many-body state Φ_0 is specified[1].

The 1–1 correspondence between time-dependent densities and time-dependent potentials can be established for any *given* interaction $\hat{W}$, in particular also for $\hat{W} \equiv 0$, i. e. for non-interacting particles. Therefore, if $n(\mathbf{r}t)$ is a *given* density,

[1] If the initial state Φ_0 is a non-degenerate ground state then the traditional Hohenberg-Kohn theorem [1] ensures that Φ_0 is a functional of the initial density n_0. Hence, in this case, Φ_0 need not be given explicitly, i. e., knowledge of n_0 is sufficient.

the potential $v(\mathbf{r}t)$ of *non-interacting* particles that reproduces the given density $n(\mathbf{r}t)$ is *uniquely* determined, $v(\mathbf{r}t) = v[n](\mathbf{r}t)$, i. e. the given density $n(\mathbf{r}t)$ can be calculated from

$$n(\mathbf{r}t) = \sum_{j=1}^{N} |\phi_j(\mathbf{r}t)|^2 \tag{13}$$

with the single-particle orbitals $\phi_j(\mathbf{r}t)$ satisfying

$$i\frac{\partial}{\partial t}\phi_j(\mathbf{r}t) = \left(-\frac{\nabla^2}{2} + v[n](\mathbf{r}t)\right)\phi_j(\mathbf{r}t) \quad . \tag{14}$$

Whether or not $v(\mathbf{r}t)$ actually *exists* for an *arbitrary* given density $n(\mathbf{r}t)$ is an open question in the time-dependent case[2]. But if it exists it is *unique*. If one chooses for $n(\mathbf{r}t)$ the density of the *interacting* system of interest (i. e. the density of Coulomb-interacting particles moving in the external potential $v_{\rm ext}(\mathbf{r}t)$) then the potential $v[n]$ is termed the time-dependent Kohn-Sham (TDKS) potential. The latter is usually decomposed into the external potential, a time-dependent Hartree part and the so-called exchange-correlation (xc) potential:

$$v[n](\mathbf{r}t) = v_{\rm ext}(\mathbf{r}t) + \int d^3r' \, \frac{n(\mathbf{r}'t)}{|\mathbf{r}-\mathbf{r}'|} + v_{\rm xc}[n](\mathbf{r}t) \quad . \tag{15}$$

The xc potential is a *universal* functional of the density, i. e. it has the *same* functional dependence on n for *all* Coulomb systems, independent of the particular external potential $v_{\rm ext}$ of the system at hand. As in the static case, the great advantage of the TDKS scheme lies in its computational simplicity compared to other methods such as TDHF or time-dependent configuration interaction. The crucial feature of $v_{\rm xc}$ is that it is a *local* potential in configuration space in contrast, e. g., to the non-local TDHF potential.

The basic formalism is easily extended to spin-polarized systems [12]. In that case the xc potential depends on the spin densities

$$n_\sigma(\mathbf{r}t) = \sum_{j=1}^{N_\sigma} |\phi_{j\sigma}(\mathbf{r}t)|^2 \quad , \quad \sigma = \uparrow\downarrow \tag{16}$$

with $N = \sum_\sigma N_\sigma$, and the spin orbitals $\phi_{j\sigma}(\mathbf{r}t)$ satisfy the single-particle equations

$$i\frac{\partial}{\partial t}\phi_{j\sigma}(\mathbf{r}t) = \left(-\frac{\nabla^2}{2} + v_\sigma[n_\uparrow, n_\downarrow](\mathbf{r}t)\right)\phi_{j\sigma}(\mathbf{r}t) \tag{17}$$

with

$$v_\sigma[n_\uparrow, n_\downarrow](\mathbf{r}t) = v_{{\rm ext}\sigma}(\mathbf{r}t) + \int d^3r' \, \frac{n_\uparrow(\mathbf{r}'t) + n_\downarrow(\mathbf{r}'t)}{|\mathbf{r}-\mathbf{r}'|} + v_{{\rm xc}\sigma}[n_\uparrow, n_\downarrow](\mathbf{r}t) \quad . \tag{18}$$

In practice, the xc potential $v_{{\rm xc}\sigma}[n_\uparrow, n_\downarrow](\mathbf{r}t)$ has to be approximated. The simplest

[2] This question is termed the *v-representability problem*. In the static case, the question could be answered in a satisfactory way. For a review of the static v-representability problem see, e. g., chapter 4.2 of Ref. [3].

possible form is the so-called adiabatic local density approximation (ALDA):

$$v_{\mathrm{xc}\sigma}^{\mathrm{ALDA}}[n_\uparrow, n_\downarrow](\mathbf{r}t) = \left.\frac{de_{\mathrm{xc}}^{hom}(n_\uparrow, n_\downarrow)}{dn_\sigma}\right|_{n_\sigma = n_\sigma(\mathbf{r}t)} \quad , \tag{19}$$

where $e_{\mathrm{xc}}^{hom}(n_\uparrow, n_\downarrow)$ is the xc energy per volume of the homogeneous spin-polarized electron gas. This approximation can be expected to be good only if the time dependence of the $n_\uparrow$ and $n_\downarrow$ is sufficiently slow. In practice, however, it gives quite good results even for cases of rather rapid time dependence. In the exchange-only case (to which we shall restrict ourselves in the following), one explicitly obtains

$$v_{\mathrm{x}\sigma}^{\mathrm{ALDA}}(\mathbf{r}t) = -\left(6n_\sigma(\mathbf{r}t)/\pi\right)^{\frac{1}{3}} \quad . \tag{20}$$

The ALDA is *local* both in space and time, i. e. $v_{\mathrm{xc}}(\mathbf{r}t)$ only depends on the density values at the very same time t and the very same location $\mathbf{r}$. Recently, a different time-dependent xc potential has been proposed which is tailored for the description of memory effects [13]. In this approximation $v_{\mathrm{xc}}(\mathbf{r}t)$ depends on the density values $n(\mathbf{r}'t')$ at other locations $\mathbf{r}'$ and earlier times $t' \leq t$. Both approximations have in common that they are based on results derived from the homogeneous electron gas.

We have recently developed a new method of constructing approximations of $v_{\mathrm{xc}\sigma}$ [8, 14, 15] which also in principle takes memory effects into account but does not make use of the theory of the homogeneous electron gas. The approach can be viewed as a time-dependent extension of the so-called optimized potential method (OPM). As before, the description of the time evolution of an N-electron system with a given initial state is made in terms of a set of time-dependent spin orbitals $\{\phi_{j\sigma}(\mathbf{r}t)\}$ obeying a single-particle Schrödinger equation analogous to Eq. (17). The difference compared to conventional density-functional schemes is that the time-dependent xc potential appearing in Eq. (18) is now given as a functional of the *orbitals* $\{\phi_{j\sigma}(\mathbf{r}t)\}$ rather than the spin densities. It is constructed by requiring the spin orbitals in Eq. (17) to make a given total quantum mechanical action functional $A[\{\phi_{j\sigma}\}]$ stationary. This condition leads to the following integral equation for the optimized xc potentials [14]:

$$i\sum_j^{N_\sigma}\int_{-\infty}^{t_1} dt' \int d^3r' \left[v_{\mathrm{xc}\sigma}^{\mathrm{OPM}}(\mathbf{r}'t')\phi_{j\sigma}^*(\mathbf{r}'t') - \frac{\delta A_{\mathrm{xc}}[\{\phi_{j\sigma}\}]}{\delta\phi_{j\sigma}(\mathbf{r}'t')}\right]\phi_{j\sigma}(\mathbf{r}t)K_\sigma(\mathbf{r}t,\mathbf{r}'t') + c.c. = 0 \tag{21}$$

with the kernel $K_\sigma(\mathbf{r}t,\mathbf{r}'t') = \sum_{k=1}^{\infty}\phi_{k\sigma}^*(\mathbf{r}t)\phi_{k\sigma}(\mathbf{r}'t')\,\theta(t-t')$. The functional $A_{\mathrm{xc}}[\{\phi_{j\sigma}\}]$ in Eq. (21) is the xc part of the total action functional and has to be approximated in practice. If all time-dependent correlation effects are neglected (x-only case) then A_{xc} is given by the usual TDHF expression

$$A_{\mathrm{x}} = -\frac{1}{2}\sum_\sigma\sum_{i,j}^{N_\sigma}\int_{-\infty}^{t_1} dt\int d^3r\int d^3r'\,\frac{\phi_{i\sigma}^*(\mathbf{r}'t)\phi_{j\sigma}(\mathbf{r}'t)\phi_{i\sigma}(\mathbf{r}t)\phi_{j\sigma}^*(\mathbf{r}t)}{|\mathbf{r}-\mathbf{r}'|} \quad . \tag{22}$$

The numerical implementation of the full time-dependent OPM scheme is an extremely demanding task: at each time step one has to solve the integral equation (21) for $v_{\mathrm{xc}\sigma}^{\mathrm{OPM}}$. For this reason, we have developed a simplified scheme similar to the one proposed by Krieger, Li and Iafrate (KLI) [16] for the static case which yields approximations to $v_{\mathrm{xc}\sigma}^{\mathrm{OPM}}$ as *explicit* functionals of the orbitals. These approximate xc potentials are given by [8, 14, 15]

$$v_{\mathrm{xc}\sigma}^{\mathrm{KLI}}(\mathbf{r}t) = w_{\mathrm{xc}\sigma}(\mathbf{r}t) + \frac{1}{n_\sigma(\mathbf{r}t)} \sum_{j,k}^{N_\sigma} n_{j\sigma}(\mathbf{r}t) \left(\Pi_\sigma^{-1}(t)\right)_{jk} \int d^3r' \, n_{k\sigma}(\mathbf{r}'t) w_{\mathrm{xc}\sigma}(\mathbf{r}'t) \quad (23)$$

with

$$\begin{aligned} w_{\mathrm{xc}\sigma}(\mathbf{r}t) = & \frac{1}{n_\sigma(\mathbf{r}t)} \sum_{j}^{N_\sigma} n_{j\sigma}(\mathbf{r}t) \, \frac{1}{2} \left(\frac{1}{\phi_{j\sigma}^*(\mathbf{r}t)} \, \frac{\delta A_{\mathrm{xc}}[\{\phi_{j\sigma}\}]}{\delta \phi_{j\sigma}(\mathbf{r}t)} + c.c. \right) \\ & - \frac{1}{n_\sigma(\mathbf{r}t)} \sum_{j}^{N_\sigma} n_{j\sigma}(\mathbf{r}t) \, \frac{1}{2} \left(\int d^3r \; \phi_{j\sigma}(\mathbf{r}t) \frac{\delta A_{\mathrm{xc}}[\{\phi_{j\sigma}\}]}{\delta \phi_{j\sigma}(\mathbf{r}t)} + c.c. \right) \\ & + \frac{i}{4n_\sigma(\mathbf{r}t)} \sum_{j}^{N_\sigma} \nabla^2 n_{j\sigma}(\mathbf{r}t) \int_{-\infty}^{t} dt' \left(\int d^3r \; \phi_{j\sigma}(\mathbf{r}t') \frac{\delta A_{\mathrm{xc}}[\{\phi_{j\sigma}\}]}{\delta \phi_{j\sigma}(\mathbf{r}t')} - c.c. \right) \quad (24) \end{aligned}$$

and $n_{j\sigma}(\mathbf{r}t) = |\phi_{j\sigma}(\mathbf{r}t)|^2$. The $N_\sigma \times N_\sigma$ matrix $\Pi_\sigma(t)$ in Eq. (23) is defined as

$$\Pi_{kj\sigma}(t) = \delta_{kj} - \int d^3r \, \frac{n_{k\sigma}(\mathbf{r}t) n_{j\sigma}(\mathbf{r}t)}{n_\sigma(\mathbf{r}t)} \quad . \quad (25)$$

The essential ingredient of the quantity $w_{\mathrm{xc}\sigma}$ is the functional derivative $\delta A_{\mathrm{xc}}/\delta \phi_{j\sigma}$ which can be calculated analytically once the approximation of A_{xc} is specified. For example, in the x-only case $w_{\mathrm{xc}\sigma}$ becomes

$$\begin{aligned} w_{\mathrm{x}\sigma}(\mathbf{r}t) = & -\frac{1}{n_\sigma(\mathbf{r}t)} \sum_{j,k}^{N_\sigma} \left[\phi_{j\sigma}(\mathbf{r}t) \phi_{k\sigma}^*(\mathbf{r}t) \int d^3r' \, \frac{\phi_{k\sigma}(\mathbf{r}'t) \phi_{j\sigma}^*(\mathbf{r}'t)}{|\mathbf{r}-\mathbf{r}'|} \right. \\ & \left. - n_{j\sigma}(\mathbf{r}t) \int d^3r \int d^3r' \, \frac{\phi_{j\sigma}(\mathbf{r}t) \phi_{k\sigma}^*(\mathbf{r}t) \phi_{k\sigma}(\mathbf{r}'t) \phi_{j\sigma}^*(\mathbf{r}'t)}{|\mathbf{r}-\mathbf{r}'|} \right] . \quad (26) \end{aligned}$$

The full x-only OPM potential constitutes the exact x-only limit of TDDFT. It is distinguished from TDHF by the fact that the OPM exchange potential is local and therefore numerically favourable. We emphasize that the x-only TDOPM should not be considered as a local approximation to TDHF. Apart from its numerical simplicity the x-only OPM is also *physically superior* to HF. This is most easily appreciated in the static limit: The static OPM orbitals (both occupied and unoccupied ones) are self-interaction free. By contrast, in HF only the occupied orbitals are self-interaction free while the unoccupied ones have a serious self-interaction error which causes them to be much too weakly bound. Since time-dependent external fields will cause transitions to the virtual orbitals (which are poorly represented in HF) we expect the x-only OPM to be more accurate than TDHF (even

if the full OPM exchange potential is approximated by the KLI potential (23)). The KLI potential (23) is significantly more accurate but also numerically more involved than the ALDA potential (20). In section 4, TDKLI results will be compared with ALDA results for neon in strong laser pulses. For these calculations, the difference in CPU time between TDKLI and ALDA is about a factor of 3. Before that, in section 3, we illustrate our numerical procedure by considering various aspects of harmonic generation in helium within a time-dependent Hartree approach.

3. Harmonic generation and two-colour mixing in helium

The initial KS ground state of He is the doubly occupied 1s orbital. In this case, there are no exchange contributions and, for the time being, the correlation part of $v_{\rm xc}$ will be neglected. The TDKLI equation (17) then reduces to the time-dependent Hartree equation

$$i\,\frac{\partial}{\partial t}\,\phi_{1s}(\mathbf{r}t) = \left(-\frac{\nabla^2}{2} + \int d^3r'\,\frac{|\phi_{1s}(\mathbf{r}'t)|^2}{|\mathbf{r}-\mathbf{r}'|} + E_0\,f(t)\,z\,\sin(\omega_0 t) - \frac{2}{r}\right)\phi_{1s}(\mathbf{r}t) \quad . \tag{27}$$

The index "1s" indicates that the time-dependent orbital $\phi_{1s}(\mathbf{r}t)$ initially was in the 1s state.

The laser field, assumed to be linearly polarized along the z direction, has been written in dipole approximation in the usual length form, with peak field strength E_0 and frequency ω_0. The envelope function, $f(t)$, is such that the laser is linearly ramped to its maximum amplitude over the first 10 cycles which is then held constant for another 10 cycles.

We solve this equation in cylindrical coordinates with a finite-difference scheme very similar to Kulander [17, 18], using a finite non-uniform grid as introduced by Pindzola *et al.* [19]. The spatial extent of the grid is about 20 a.u. × 60 a.u., and the initial helium ground state has an energy eigenvalue of $\epsilon_{1s} = -0.955$ Hartrees which is 3.9% off the exact Hartree-Fock value of -0.918 Hartrees. This error is due to the relatively coarse grid spacings in the vicinity of the nucleus, which is inevitable to keep the numerical effort tractable.

We simulate ionization by an absorbing grid boundary [17, 18] so that the norm of the wave function

$$N_{1s}(t) = \int\limits_{\substack{\text{finite}\\ \text{volume}}} d^3r\,|\phi_{1s}(\mathbf{r}t)|^2 \quad , \tag{28}$$

taken over the finite volume of the grid, decreases with time. The time-dependent norm $N_{1s}(t)$ refers to a singly occupied spin orbital. The probabilities for neutral, singly and doubly charged helium atoms can therefore be expressed as

$$P^0(t) = N_{1s}(t)^2 \tag{29}$$

$$P^{+1}(t) = 2N_{1s}(t)(1-N_{1s}(t)) \tag{30}$$

$$P^{+2}(t) = (1-N_{1s}(t))^2 \quad . \tag{31}$$

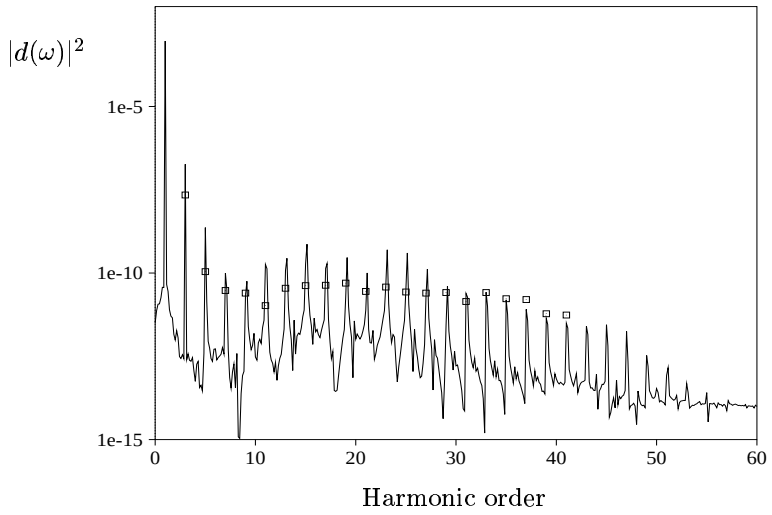

Figure 1: *Harmonic spectrum for He at* $\lambda = 616$nm *and* $I = 3.5 \times 10^{14}$ W/cm^2. *The squares represent experimental data taken from Ref. [20] normalized to the value of the 33rd harmonic of the calculated spectrum. The experiment was performed with a peak intensity of* 1.4×10^{14}W/cm^2.

Since $N_{1s}(t) = \int d^3r\ n(\mathbf{r}t)/2$, the probabilities P^0, P^{+1} and P^{+2} as given by Eqs. (29)–(31) are explicit functionals of the density.

In order to investigate harmonic generation for the helium atom, we take the laser wave length 616 nm, which has been used for an experimental study by Miyazaki and Sakai [20]. They employed a dye laser with a pulse duration of 800 femtoseconds and a peak intensity of 1.4×10^{14} W/cm^2. The highest detected harmonic was the 41st, corresponding to a wavelength of 15 nm.

To obtain the harmonic spectrum, we calculate the induced dipole moment $d(t) = \int d^3r\ z\, n(\mathbf{r}t)$ which is then Fourier transformed over the last 5 cycles of the constant-intensity interval. The square of the resulting Fourier transform, $|d(\omega)|^2$, has been shown [21] to be proportional to the experimentally observed harmonic distribution to within a very good approximation.

We performed calculations with different peak intensities and achieved the best agreement with experiment for $I = 3.5 \times 10^{14}$ W/cm^2, see Fig. 1. The discrepancy between this intensity and the experimental intensity of 1.4×10^{14} W/cm^2 might be due to the uncertainty of the experimentally determined peak intensity which can be as high as a factor of two.

To explain experimental harmonic generation data, Lambropoulos and coworkers [22] have performed numerical simulations for helium based on a single-active-electron model. Their aim was to clarify the role of He^{+1} in the harmonic generation process at different laser wavelengths. For this purpose, they calculated the harmonic spectra separately for neutral helium and for He^{+1} at the respective saturation intensities (i. e. those intensities for which about 5% of the populations of

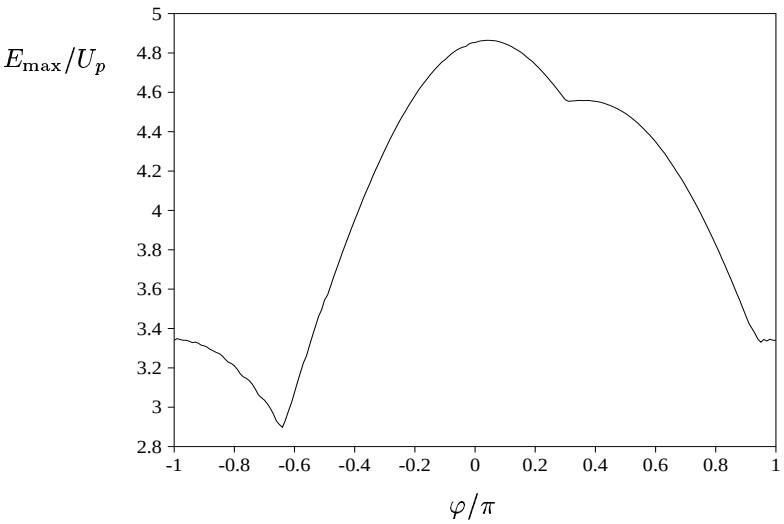

Figure 2: *Maximum return energy of a classical electron released from the nucleus in a two-colour laser field with a relative phase difference φ.*

the He atom or the ion are ionized during the laser pulses). The spectra were then compared with experiment in order to find out which part of the detected harmonic spectrum was caused by neutral He and which part by singly charged He. This method explains quite well an experiment performed at the wavelength 248 nm [23], but does not give a clear picture for the experimental data of Miyazaki and Sakai [20] at 616 nm: for the latter case, the intensities ($5 \times 10^{14}\,\mathrm{W/cm^2}$ for neutral He and $5 \times 10^{15}\,\mathrm{W/cm^2}$ for He^{+1}) leading to good agreement with experiment were out of the range of the experimental peak intensity of $1.4 \times 10^{14}\,\mathrm{W/cm^2}$.

If we calculate the probabilities for the charge states of He at 616 nm and $3.5 \times 10^{14}\,\mathrm{W/cm^2}$ after 20 cycles by using Eqs. (29)–(31), we obtain 99.93% probability for neutral He and only 0.07% for He^{+1}. We thus conclude that the spectrum shown in Fig. 1 is exclusively due to the neutral atom.

We also studied the harmonic generation for a helium atom in a strong two-colour laser field. The two lasers with frequencies ω_0 and $2\omega_0$, respectively, are operated with the same peak intensity and a constant relative phase difference φ. This results in a time-varying laser potential of the form

$$v_{\mathrm{laser}}(\mathbf{r}t) = E_0 f(t) z[\sin(\omega_0 t) + \sin(2\omega_0 t + \varphi)] \quad , \tag{32}$$

where both fields are linearly polarized along the z-axis. One expects to obtain harmonic distributions with a plateau region extending up to a cutoff which depends on the phase difference φ. In the one-colour case, this cutoff is approximately determined by the well-known $I_p + 3.2U_p$ rule [24], where I_p denotes the atomic ionization potential and U_p the ponderomotive shift.

To obtain an analogous rule for the two-colour case, we have calculated the maximum return energies $E_{\max}$ for a classical electron released at the nucleus in a

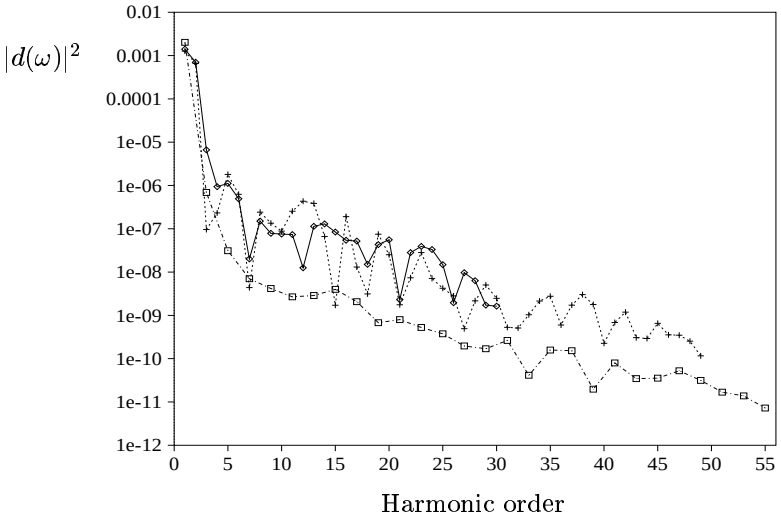

Figure 3: *Harmonic distribution for He in a two-colour laser field. The two wavelengths are* 616 nm *and* 308 nm, *and the intensity is* 3.5×10^{14} W/cm^2 *for both of them. Crosses are the results for* $\varphi = 0$ *and diamonds denote the values obtained with phase shift* $\varphi = -0.6\pi$. *For comparison, the squares indicate the harmonic distribution for He in a one-colour field with* $\lambda = 616$ nm *and* $I = 7 \times 10^{14}$ W/cm^2.

two-colour laser field. The cutoff is then given by $I_p + E_{\max}$. In Fig. 2, $E_{\max}/U_p$ is plotted as a function of the phase shift, where U_p is now given by the sum of the ponderomotive potentials of the two individual laser fields. We have made several calculations for laser intensities in the range of 10^{13} to 10^{15} W/cm^2 and wavelengths between 200 and 1200nm. The curve plotted in Fig. 2 turned out to be insensitive to these variations of the laser parameters. The two-colour cutoff rule can thus be written as $I_p + c(\varphi)U_p$, where $c(\varphi) = E_{\max}/U_p$ has its maximum value of about 4.9 for $\varphi = 0$, whereas it has a minimum of about 2.9 for $\varphi = -0.64\pi$.

Calculated harmonic distributions induced by a two-colour field with different relative phases are shown in Fig. 3. The fundamental wave length is 616 nm and the intensity is 3.5×10^{14} W/cm^2 for both frequency components. We also show the one-colour spectrum for $\lambda = 616$ nm calculated with the *same* total intensity as the two-colour field, i. e. $I = 7 \times 10^{14}$ W/cm^2. In the two-colour spectrum, harmonics at all higher multiples (including even multiples) of the fundamental frequency ω_0 occur due to nonlinear mixing processes of the two fields [25]. We chose the phase differences $\varphi = 0$ and $\varphi = -0.6\pi$ which according to our semiclassical model (see Fig. 2) lead to the highest and lowest cutoff energies, namely the 50th harmonic and the 36th harmonic, respectively. These classical estimates are found to agree quite well with the full quantum mechanical calculations: for $\varphi = 0$ we observe harmonics as high as the 49th, whereas for $\varphi = -0.6\pi$ we find the plateau to extend up to the 30th harmonic.

In Fig. 3, most of the harmonics produced by the two-colour field in the plateau region are one to two orders of magnitude more intense than those obtained in the one-colour calculation. Similar results have recently been found for hydrogen in a two-colour field [26]. One possible reason for this remarkable enhancement is that in a two-colour field one specific high-order harmonic can be generated by a large number of different mixing processes [25]. Several of the two-colour harmonics, on the other hand, are found to be strongly suppressed: the 7th and 15th harmonics for the case $\varphi = 0$, e. g., are even below their counterparts calculated in the one-colour field. For $\varphi = -0.6\pi$, however, this suppression of the 15th harmonic does not occur. Other harmonics like the 12th are enhanced for $\varphi = 0$ and suppressed for $\varphi = -0.6\pi$.

4. Neon: beyond the single-active-electron approximation

For atoms heavier than He, exchange terms are present in the TDKS equations. In this section we present a full TDDFT calculation for the neon atom. We have solved the TDKS equations with the TDKLI and ALDA potentials for the Ne valence electrons in a laser pulse with $\lambda = 248$ nm for two different intensities, $I = 3 \times 10^{15}$ W/cm^2 and 5×10^{15} W/cm^2. The 1s electrons have been frozen, i. e. we propagate only the 2s and 2p electrons by solving the TDKS equations, whereas the time evolution of the 1s electrons is given by

$$\phi_{1s}(\mathbf{r}t) = \phi_{1s}(\mathbf{r}t_0)\, e^{-i\epsilon_{1s}(t-t_0)} \quad . \tag{33}$$

We emphasize that the only approximation made in this frozen-core prescription is to write the frozen orbitals in the form (33). The exchange between the frozen orbitals and the other orbitals is fully included in the TDKLI or ALDA potentials. In this respect, our scheme differs from other frozen-core prescriptions such as, e. g., in Ref. [24]. In view of the high binding energy of the 1s electrons compared

	$\mathrm{HF}^{(\mathrm{exact})}$	$\mathrm{KLI}^{(\mathrm{exact})}$	$\mathrm{LDA}^{(\mathrm{exact})}$	$\mathrm{KLI}^{(\mathrm{grid})}$	$\mathrm{LDA}^{(\mathrm{grid})}$
$-\epsilon_{1s}$	32.77	30.80	30.24	35.13	34.47
$-\epsilon_{2s}$	1.930	1.707	1.266	1.951	1.522
$-\epsilon_{2p_0}$	0.8504	0.8494	0.4431	0.8098	0.4159
$-\epsilon_{2p_1}$	0.8504	0.8494	0.4431	0.8065	0.4126

Table 1: *Ne orbital energies (in Hartrees).*

to the other electrons (see Table 1), freezing only the 1s electrons is expected to be a very good approximation for the neon atom. Later we shall discuss the effect of additionally freezing electrons of the valence shell and only propagating the most loosely bound, i. e. the $2p_0$ orbital.

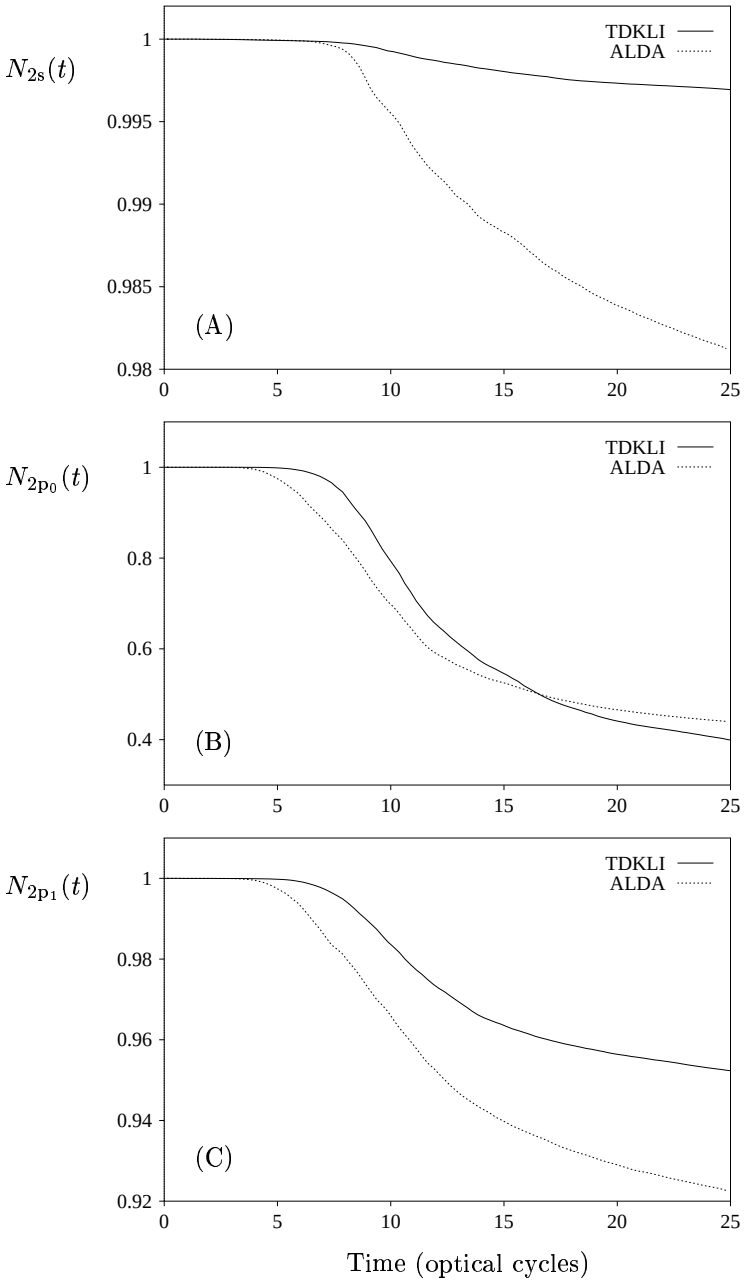

Figure 4: *Time evolution of the norm of the Ne 2s orbital (A), the Ne* $2p_0$ *orbital (B) and the Ne* $2p_1$ *orbital (C), calculated in the x-only TDKLI and ALDA schemes. Laser parameters:* $\lambda = 248\,\mathrm{nm}$, $I = 3 \times 10^{15}\,\mathrm{W/cm^2}$, *linear ramp over the first 10 cycles. One optical cycle corresponds to 0.82 femtoseconds.*

In order to assess the accuracy of the numerical procedure we first compare the energy eigenvalues resulting from the diagonalization of the stationary KS equation on our two-dimensional grid with the exact values from the literature [16, 27, 28], see Table 1. We find that there is a slight difference (about 3 mHartrees) between the eigenvalues of the $2p_0$ and $2p_1$ orbitals due to the different orientations of these orbitals in our cylindrical grid: the $2p_0$ orbital is oriented along the z-axis, the $2p_1$ orbitals perpendicular to it. In the limit of infinitesimally small grid spacings, this difference goes to zero. The deviation of the average of the 2p orbital energies from the exact value is 4.9% (41 mHartrees) for KLI and 6.5% (29 mHartrees) for LDA. The KLI results for the orbital binding energies (on the exact level as well as calculated on the rectangular grid) are found to be much closer to the HF results than the LDA energy eigenvalues. The first ionization potential of Ne in LDA is too small by almost 50%, whereas the exact KLI result reproduces the HF ionization potential within 1 mHartree (0.1%). We mention that the experimental ionization potential is 0.792 Hartrees.

Fig. 4 shows the norm of the Ne 2s, $2p_0$ and $2p_1$ orbitals for the laser intensity $I = 3 \times 10^{15}$ W/cm^2 (a very similar behaviour is found for $I = 5 \times 10^{15}$ W/cm^2). Once again the indices "2s", "$2p_0$" and "$2p_1$" denote the *initial* state of the otherwise fully propagated orbitals. The pulse has been linearly ramped over the first ten cycles and is then kept constant for another 15 cycles. As expected, the 2s orbital is the least ionized of the three orbitals (only 0.3% ionization for TDKLI and 1.9% for ALDA at the end of our calculation). A little surprising at first sight, the $2p_0$ and $2p_1$ orbitals differ by about an order of magnitude in their degree of ionization (60% for the $2p_0$ orbital compared to only 4.75% for the $2p_1$ orbital within TDKLI, and 56% for the $2p_0$ compared to 7.7% for the $2p_1$ orbital within the ALDA). This difference has been observed before by Kulander [29, 30] for the case of xenon (in a single-active-electron calculation). It is due to the fact that the $2p_0$ orbital is oriented along the polarization direction of the laser field, which makes it easier for the electrons to escape the nuclear attraction than for the case of the $2p_1$ orbital, which is oriented perpendicularly to the field polarization.

To explain the difference between the results obtained within the TDKLI and ALDA schemes shown in Fig. 4, we observe from Table 1 that it takes 5 photons to ionize the 2p orbitals in TDKLI compared to only 3 photons in ALDA. Similarly, it takes 11 photons to ionize the 2s orbital in TDKLI and only 9 in ALDA. The difference between the curves in Fig. 4A and C is thus hardly surprising. On the other hand, it seems quite unexpected that the ALDA and TDKLI curves cross in Fig. 4B so that the ALDA curve comes to lie *above* the TDKLI curve. This behaviour can be attributed to the fact that the other orbitals are ionized much more strongly in ALDA than in TDKLI, so that their electron density near the nucleus (and therefore their screening of the nuclear charge) is decreased. This makes it more difficult for the $2p_0$ electrons to escape within the ALDA scheme.

We have calculated the harmonic spectra for both sets of laser parameters. The distributions are displayed in Figs. 5A and B. We see that for the lower intensity, $I = 3 \times 10^{15}$ W/cm^2, the plateau extends up to the 23rd harmonic, whereas for $I = 5 \times 10^{15}$ W/cm^2 it goes up to the 33rd harmonic. We also observe that the

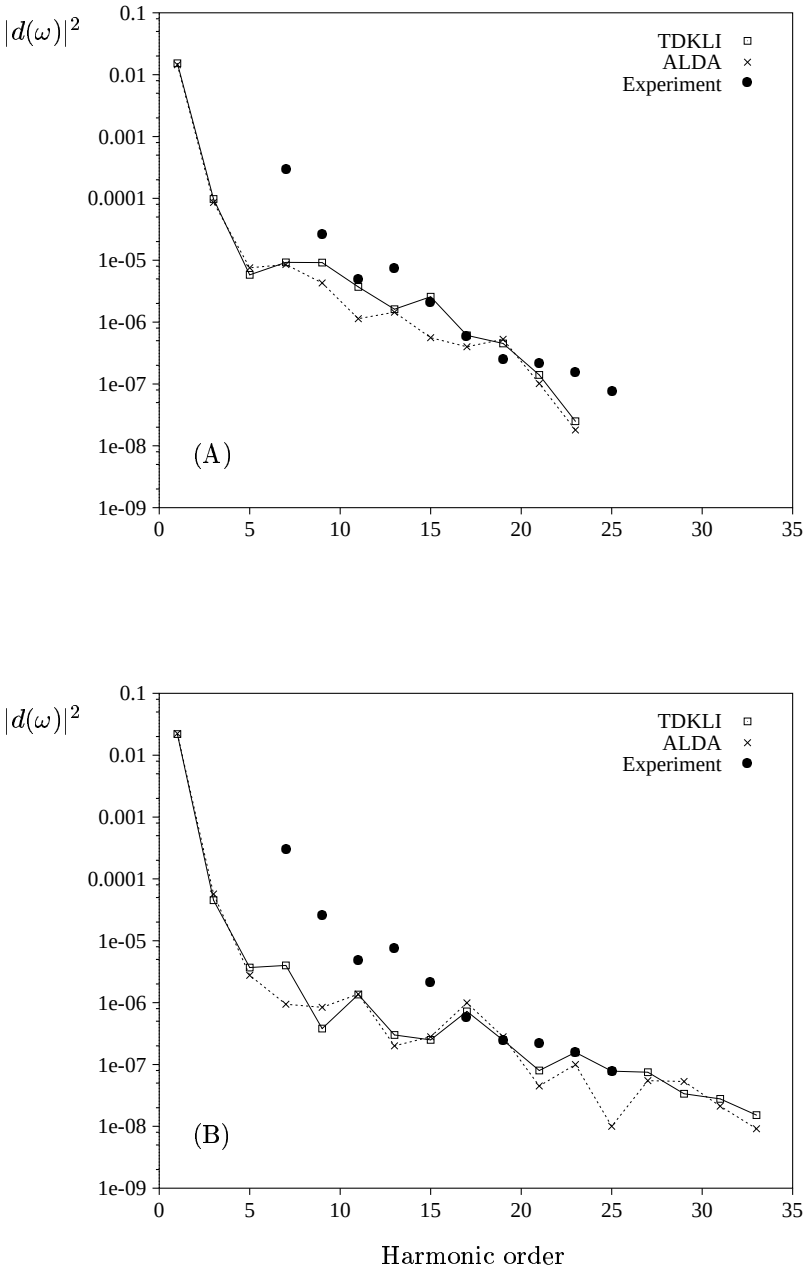

Figure 5: *Harmonic distributions for Ne* ($\lambda = 248$ nm)*, calculated within the TDKLI and ALDA schemes at* $I = 3 \times 10^{15}$ W/cm^2 *(A) and* $I = 5 \times 10^{15}$ W/cm^2 *(B). The experimental data were taken at* $I = 4 \times 10^{17}$ W/cm^2 *[23].*

difference between the TDKLI and ALDA spectra is not very pronounced. We thus conclude that the strongly differing ionization energies of the individual orbitals (a factor of two for the 2p electrons) play only a minor role for the shape of the harmonic spectrum.

We compare our calculated harmonic distributions with experimental data by Sarukura *et al.* [23]. The experiment was performed with a KrF laser (λ = 248 nm) at a pulse duration of 280 femtoseconds and a peak intensity of 4×10^{17} W/cm^2. The experimental peak intensity is two orders of magnitude higher than the intensities used in our calculations. It is to be expected, however, that the atoms have become completely ionized by the time the pulse reaches its maximum. The detected harmonic radiation must therefore have been induced during the rise time of the pulse, probably in an intensity range close to the intensities used in our calculations.

The experimental data points shown in Figs. 5A and B have both been normalized to the value of the 17th harmonic (within TDKLI) in Fig. 5A. At 3×10^{15} W/cm^2, we see that the calculated spectra can explain the measured harmonics 15 to 21, whereas the harmonics 17 to 25 (with the exception of the strongly suppressed 25th harmonic for ALDA and the a little less strongly suppressed 21st harmonic for both schemes) are explained by the spectrum at 5×10^{15} W/cm^2. Hence, our calculations show that the generation of the harmonics 15 to 25 is dominated by the intensity range covered in our calculations. We can match this part of the experimental harmonic distribution pretty well by a superposition of the two spectra with equal weights. This corresponds to the experimental situation where the harmonic photons generated on different positions in the laser focus (and, therefore, coming from regimes with different laser intensities) are superimposed in the detector.

In order to explain the same experimental data, Kondo *et al.* [31] have performed numerical simulations based on a simple atomic model (a single electron in a short-range model potential). They calculated the harmonic spectrum for neutral Ne at 4.5×10^{14} W/cm^2, for Ne^{+1} at 1.8×10^{15} W/cm^2 and for Ne^{+2} at 4.8×10^{15} W/cm^2. By a suitable superposition of these single-electron spectra, they reproduced the qualitative features of the experimental harmonic distribution. The authors attributed the harmonics above the 11th to Ne^{+1} and the harmonics above the 21st to doubly charged Ne.

We come to a similar conclusion by calculating the populations of the differently charged states as we did for the helium atom, see Eqs. (29)–(31). For the intensity 3×10^{15}W/cm^2, we find a slightly higher probability for Ne^{+1} than for Ne^{+2}. Thus, the harmonics up to the 21st are most probably caused by Ne^{+1}. At the higher intensity, we find that the doubly charged Ne ions are prevailing. We can therefore attribute the harmonics above the 21st to Ne^{+2}, in accordance with Ref. [31].

We also found that the dipole moment of the $2p_0$ orbital alone leads to spectra looking very similar to the full harmonic spectra displayed in Figs. 5A and B. This brings us to the following question: To what extent is the harmonic motion of the $2p_0$ electrons influenced by the motion of the other electrons? In order to study this question, we have performed an additional TDKLI calculation with the same

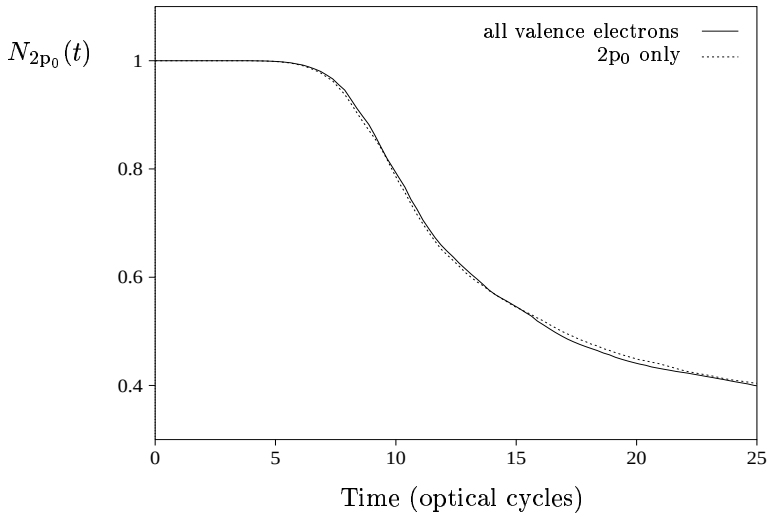

Figure 6: *Time-dependent norm of the $2p_0$ orbital, calculated with TDKLI in two different schemes (propagation of all valence electrons and of the $2p_0$ orbital only, respectively). The laser parameters are $\lambda = 248\,\mathrm{nm}$ and $I = 3 \times 10^{15}\,\mathrm{W/cm^2}$.*

laser parameters as in Fig. 5A, this time with all but the $2p_0$ electrons frozen in their initial states. Fig. 6 shows a comparison of the time-dependent norm of the $2p_0$ orbital calculated in the original scheme (i. e. all electrons are propagated under the influence of the laser except the 1s electrons) and in the new frozen-core scheme (i. e. propagation of the $2p_0$ orbital only). The difference between the two curves is very slight, implying that the *ionization* of the $2p_0$ orbital can reliably be calculated with the new frozen-core prescription.

However, if we calculate the *harmonic spectrum* in the new frozen-core scheme, we find a strong deviation from the spectrum calculated in the original scheme. From the comparison of the two spectra in Fig. 7, we come to the conclusion that the effect of freezing the 2s and $2p_1$ electrons is twofold: First of all, the whole spectrum is slightly shifted towards lower values of $|d(\omega)|^2$. The second, more drastic effect is the appearance of a pronounced Lorentz-profile resonance peak just below the 7th harmonic. This resonance dominates the background of the spectrum, as becomes clearly visible in the region beyond the plateau, i. e. beyond the 21st harmonic, which can be fitted very well with a Lorentz curve. A very similar resonance phenomenon has been observed by Kulander and Shore [30] for the case of Xenon, where a single $5p_0$ electron was propagated only.

In the former computational scheme, where all valence electrons of the neon atom were fully propagated, the resonance had been suppressed due to the influence of the 2s and $2p_1$ electrons on the motion of the $2p_0$ electrons. In other words, the resonance is an *artefact* of the more restricted frozen-core approximation, where only the $2p_0$ orbital was propagated. This leads us to the conclusion that a reliable calculation of harmonic spectra requires simultaneously treating

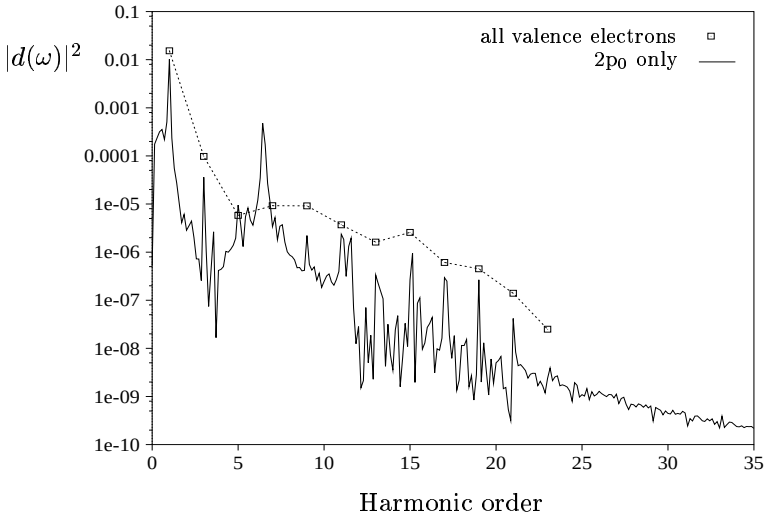

Figure 7: *Harmonic spectrum of Ne calculated by propagating the $2p_0$ orbital only. Squares: harmonic distribution calculated by propagating all valence electrons (both calculations were done in TDKLI). Laser parameters as in Fig. 6.*

the time evolution of *all* electrons belonging to the outermost atomic shell. Neglecting the mutual influence of the electrons on their harmonic motion, as done in the single-active-electron approximation, can lead to spurious resonance effects.

Acknowledgments

This work was supported in part by the Deutsche Forschungsgemeinschaft. We thank the Rechenzentrum der Universität Würzburg and the Landesrechenzentrum München for making their facilities available. S. E. and C. A. U. acknowledge with thanks a fellowship of the Studienstiftung des deutschen Volkes.

References

[1] P. Hohenberg and W. Kohn, Phys. Rev. **136**, B864 (1964)

[2] W. Kohn and L. J. Sham, Phys. Rev. **140**, A1133 (1965)

[3] R. M. Dreizler and E. K. U. Gross, *Density Functional Theory: An Approach to the Quantum Many-Body Problem* (Springer-Verlag, Berlin, 1990)

[4] *Density Functional Theory*, ed. by E. K. U. Gross and R. M. Dreizler, NATO ASI series B337 (Plenum Press, New York, 1994)

[5] T. Grabo and E. K. U. Gross, Chem. Phys. Lett. (1995), in press

[6] E. Runge and E. K. U. Gross, Phys. Rev. Lett. **52**, 997 (1984)

[7] E. K. U. Gross and W. Kohn, Adv. Quant. Chem. **21**, 255 (1990)

[8] E. K. U. Gross, C. A. Ullrich, and U. J. Gossmann, in Ref. [4], p. 149

[9] G. D. Mahan and K. R. Subbaswamy, *Local Density Theory of Polarizability* (Plenum Press, New York, 1990)

[10] *Atoms in Intense Laser Fields*, ed. by M. Gavrila (Academic Press, Boston, 1992)

[11] *Super-Intense Laser-Atom Physics*, ed. by B. Piraux, A. L'Huillier and K. Rzążewski, NATO ASI Series B316 (Plenum Press, New York, 1993)

[12] K. L. Liu and S. H. Vosko, Can. J. Phys. **67**, 1015 (1989)

[13] M. Bünner, J. F. Dobson, and E. K. U. Gross, to be published

[14] C. A. Ullrich, U. J. Gossmann, and E. K. U. Gross, Phys. Rev. Lett. **74**, 872 (1995)

[15] C. A. Ullrich, U. J. Gossmann, and E. K. U. Gross, Ber. Bunsenges. Phys. Chem. **99**, 488 (1995)

[16] J. B. Krieger, Y. Li, and G. J. Iafrate, Phys. Rev. A **45**, 101 (1992)

[17] K. C. Kulander, Phys. Rev. A **35**, 445 (1987)

[18] K. C. Kulander, Phys. Rev. A **36**, 2726 (1987)

[19] M. S. Pindzola, T. W. Gorczyca, and C. Bottcher, Phys. Rev. A **47**, 4982 (1993)

[20] K. Miyazaki and H. Sakai, J. Phys. B: At. Mol. Opt. Phys. **25**, L83 (1992)

[21] A. L'Huillier, L. A. Lompré, G. Mainfray, and C. Manus, in Ref. [10], p. 139

[22] H. Xu, X. Tang, and P. Lambropoulos, Phys. Rev. A **46**, R2225 (1992)

[23] N. Sarukura, K. Hata, T. Adachi, R. Nodomi, M. Watanabe, and S. Watanabe, Phys. Rev. A **43**, 1669 (1991)

[24] K. C. Kulander, K. J. Schafer, and J. L. Krause, in Ref. [11], p. 95

[25] H. Eichmann, A. Egbert, S. Nolte, C. Momma, and B. Wellegehausen, W. Becker, S. Long, and J. K. McIver, Phys. Rev. A **51**, R3414 (1995)

[26] M. Protopapas, A. Sanpera, P. L. Knight, and K. Burnett, Phys. Rev. A **52** (1995) (in press)

[27] E. Clementi and C. Roetti, At. Data Nucl. Data Tables **14**, 177 (1974)

[28] T. Grabo, private communication

[29] K. C. Kulander, Phys. Rev. A **38**, 778 (1988)

[30] K. C. Kulander and B. W. Shore, J. Opt. Soc. Am. B **7**, 502 (1990)

[31] K. Kondo, T. Tamida, Y. Nabekawa, and S. Watanabe, Phys. Rev. A **49**, 3881 (1994)